PHYSICAL REVIEW B VOLUME 30, NUMBER 6 15 SEPTEMBER 1984

Phonon focusing in piezoelectric crystals: Quartz and lithium niobate

G. L. Koos and J. P. Wolfe
Physics Department and the Materials Research Laboratory, University of Illinois at Urbana—Champaign, Urbana Illinois 61801

(Received 2 April 1984)

The propagation of ballistic heat pulses at low temperature in α-quartz (SiO_2) and lithium niobate ($LiNbO_3$) is characterized both experimentally and theoretically. The phonon-imaging method is used to determine the ballistic heat flux emanating from a point source. Both crystals exhibit large flux anisotropies due to phonon focusing. It is well known that such patterns arise from elastic anisotropy. The aim of this paper is to show how the heat flux is affected by the inherent piezoelectricity of these crystals. We have extended the usual calculation of phonon focusing to include the effect of piezoelectricity in the quasistatic limit by introducing "stiffened" elastic constants into the standard calculation of phonon flux. The resulting theoretical images agree quite well with experiment and show that while the effect of piezoelectricity on phonon focusing is small in α-quartz, it is dramatic in lithium niobate. A theoretical study is included which shows the interesting topological changes in the slowness and wave surfaces in lithium niobate as piezoelectric stiffening is gradually (hypothetically) introduced.

I. INTRODUCTION

The study of ballistic heat-pulse propagation through anisotropic materials at low temperatures has been greatly expanded through the use of phonon-imaging techniques.[1–3] It has been found that even in slightly anisotropic materials a heat pulse generated at a point on one crystal surface displays a very nonuniform angular distribution of phonon flux through the sample. Along certain directions the phonon flux is predicted to be mathematically infinite. Patterns of these singularities, already observed in a number of insulating and semiconducting crystals, have been well explained in terms of elasticity theory for an anisotropic medium.

The phonon-flux anisotropy is largely due to a bulk effect known as "phonon focusing." This effect occurs because the phonon wave vector and its corresponding group-velocity vector are not in general parallel. As originally shown by Taylor, Maris, and Elbaum,[4] this leads to a very pronounced directional dependence on the phonon energy flux even with a uniform distribution of phonon wave vectors.

A technique for directly imaging the ballistic phonon flux was developed by Northrop and Wolfe.[1] In this phonon-imaging method, a focused laser beam is raster-scanned across the surface of the crystal and the resulting variation in heat pulse is detected by a small fixed bolometer on the opposite surface. Recently, scannable electron beams have also been used as the heat source.[2] So far, phonon-imaging methods have been used to characterize the dispersion of large-k phonons[5] in Ge and GaAs, observe phonon-dislocation interactions[6] in LiF, and study the scattering of high-frequency phonons at sapphire interfaces.[7,8]

Invariably, the experimental images of ballistic heat flux have been analyzed in terms of previously measured elastic constants of the crystal. By solving the Christoffel equation for a given phonon energy the $\omega(\vec{k})$ relations are obtained for each of three phonon modes. The constant-frequency surfaces in wave-vector space and the wave surfaces of all possible group velocities are useful constructions in understanding the details of the phonon-focusing patterns. As an additional theoretical step, a Monte-Carlo calculation can be carried out in which a uniform distribution of phonon wave vectors is transformed into the corresponding nonuniform distribution of group-velocity vectors, giving the real-space distribution of phonon flux.

In this paper we report the results of such phonon-focusing calculations and phonon-imaging experiments on α-quartz and lithium niobate. We have chosen these crystals both because of their technological importance and also to test the effects of piezoelectricity on phonon focusing. We have extended the phonon-focusing calculation to include the piezoelectric effect in the quasistatic limit through the use of directionally-dependent "stiffened" elastic constants. The resulting calculated distributions are found to compare favorably with experimental images. Indeed, for lithium niobate there are remarkable differences in the wave surfaces and flux patterns predicted for unstiffened versus piezoelectrically stiffened elastic constants. Thus, our study shows a profound influence of piezoelectricity on ballistic heat flux in this crystal.[9]

II. PHONON-FOCUSING THEORY

A. Basic considerations

Continuum elasticity theory[10] is used to predict phonon focusing in the limit where phonon wavelengths are much larger than the lattice constant. For a nonpiezoelectric material the problem begins with the generalized Hooke's Law

$$\sigma_{ij}=C_{ijmn}S_{mn} , \qquad (1)$$

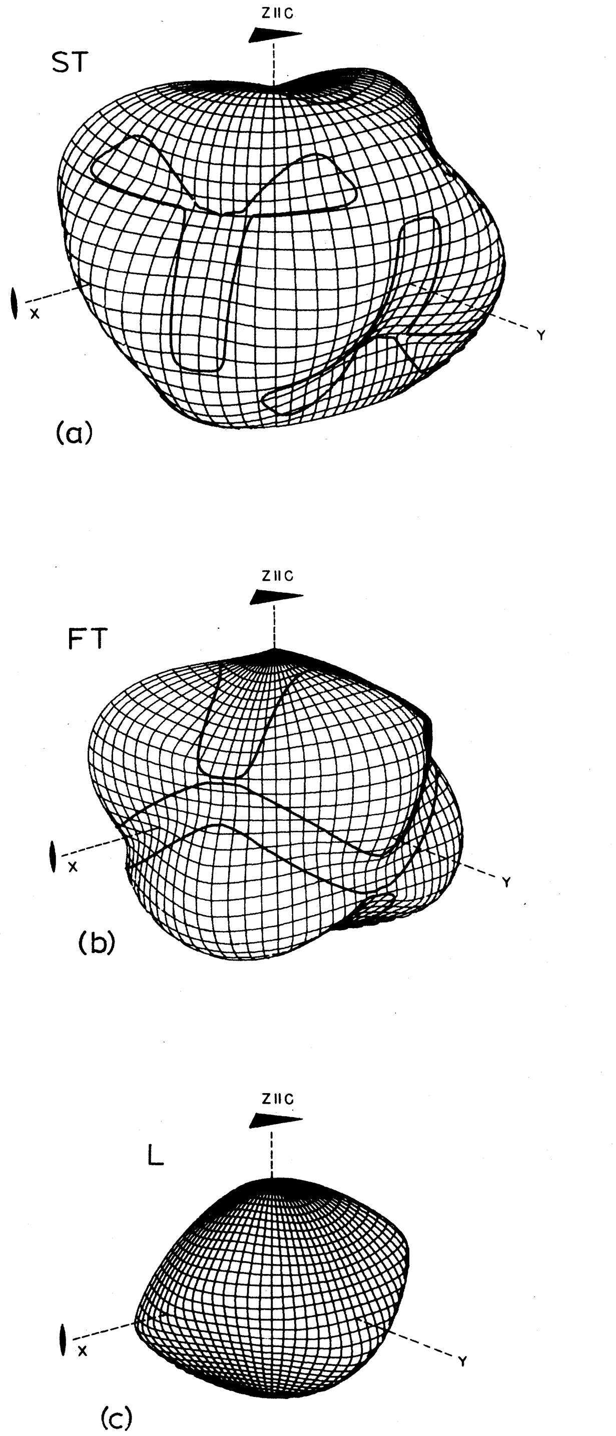

FIG. 1. Constant-frequency (or slowness) surface for α-quartz. The slowness surface obtained by using the constant-field elastic constants in Eq. (1) are not noticeably different from those obtained by using the properly stiffened constants in Eq. (13). The grid of lines define constant θ_k and ϕ_k at five-degree intervals in the range $-30° \leq \phi_k \leq 150°$ and $0° \leq \theta_k \leq 160°$. The thick lines indicate where surfaces have zero Gaussian curvature. The z and x axes are the threefold and twofold symmetric axes of the crystal. (a) The ST sheet. (b) The FT sheet. (c) The L sheet.

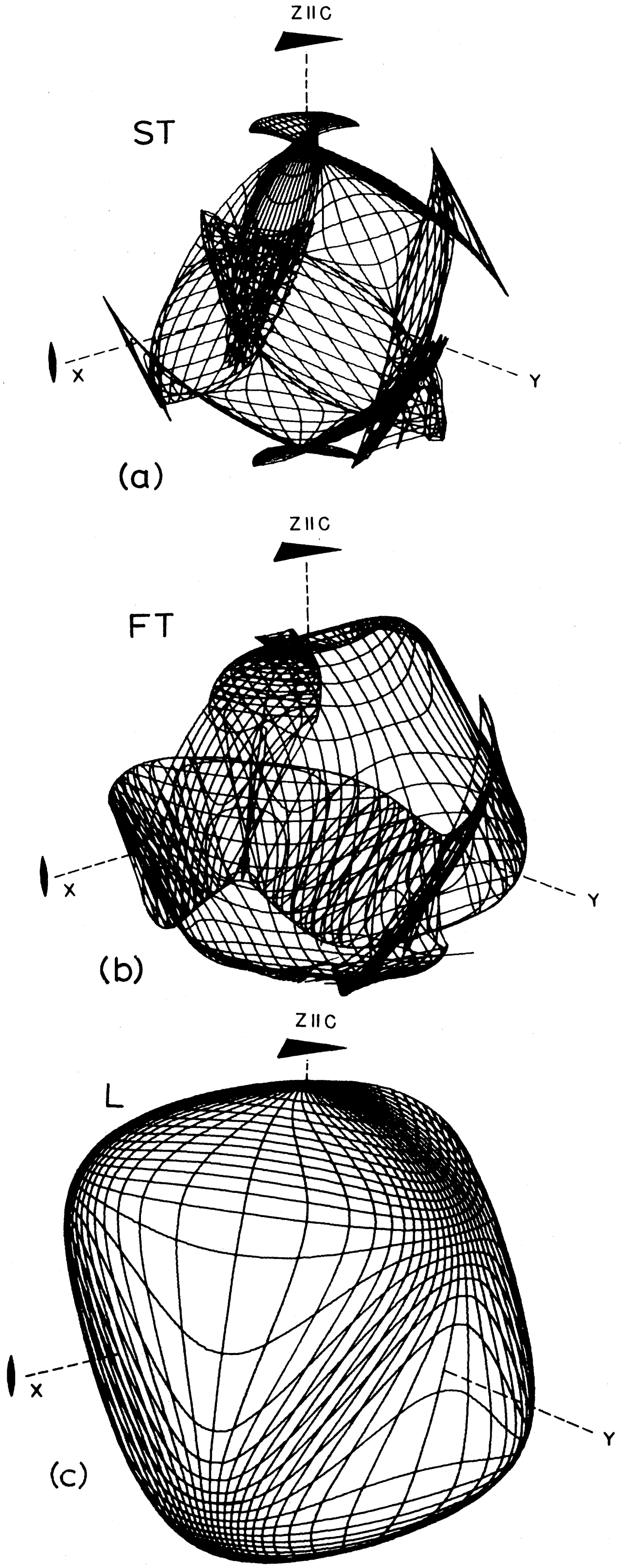

FIG. 2. Wave surface for α-quartz consisting of group-velocity vectors associating with the set of wave vectors shown in Fig. 1. The fold edges of this surface correspond to the lines of zero Gaussian curvature in Fig. 1. (a) The ST sheet. (b) The FT sheet. (c) The L sheet.

TABLE I. Elastic stiffness constants for α-quartz (Ref. 11) and lithium niobate (Ref. 12) in units of 10^{10} dyn/cm^2.

Material	C_{11}^E	C_{12}^E	C_{13}^E	C_{14}^E	C_{33}^E	C_{44}^E
α-quartz (4 K)	86.103	10.43	12.894	-17.206	108.552	59.215
lithium niobate (300 K)	203	57.3	75.2	8.5	242.4	59.5

where σ_{ij} is the stress applied in the ith direction to the jth plane, C_{ijmn} are the elastic stiffness constants,

$$S_{mn} \equiv \frac{1}{2}\left[\frac{\partial u_n}{\partial x_m} + \frac{\partial u_m}{\partial x_n}\right]$$

is the strain tensor, and $\vec{u}$ is the displacement from equilibrium at position $\vec{x} = (x_1, x_2, x_3)$.

For a crystal of density ρ, the equation of motion,

$$\rho \frac{\partial^2 u_i}{\partial t^2} = \frac{\partial \sigma_{ij}}{\partial x_j} , \tag{2}$$

has a plane-wave solution,

$$\vec{u} = \vec{u}_0 e^{i(\omega t - \vec{k}\cdot\vec{x})} , \tag{3}$$

which yields the Christoffel equation,

$$(C_{ijmn} k_j k_m - \rho\omega^2 \delta_{in}) u_n = 0 . \tag{4}$$

The solution of this equation for a given phonon frequency ω results in three sheets of allowed wave vectors corresponding to the longitudinal (L), slow transverse (ST), and fast transverse (FT) phonon modes. Figure 1 shows these three constant-frequency surfaces for α-quartz, based on the constant-field elastic constants given in Table I. This simplified use of the constant-field elastic constants was the procedure employed by Rosch and Weis,[13] who calculated a pseudo-three-dimensional representation of the phonon flux well before any phonon-imaging experiments were demonstrated. The proper inclusion of piezoelectricity, as discussed below, greatly complicates the calculation, but it turns out that for quartz the simplified use of constant-field elastic constants yields a good approximation to the actual flux distribution.

Quartz has trigonal symmetry (D_3), implying that there are six independent elastic constants. We have used the values of Smagin *et al.*[11] which were measured at low temperature by the resonance method. The transverse surfaces, as shown in Figs. 1(a) and 1(b) are highly nonspherical, and the thick lines represent the locus of points where the Gaussian curvature K vanishes. These lines separate convex and saddle regions of the surface. Noting that the group-velocity vector $\vec{V} = \vec{\nabla}_k \omega$ corresponding to a given wave vector is normal to the slowness surface at that point, it follows that along the $K = 0$ lines, a mathematically singular concentration of group-velocity vectors results.

The locus of group-velocity directions corresponding to these $K = 0$ lines can be calculated, and projected onto the experimental surface, forming a singularity pattern for the crystal [see Figs. 3(c) and 4(c)]. Another way of seeing this pattern is to plot the surface of all group-velocity vectors, or wave surface, which is shown in Fig. 2 for the three modes in α-quartz. Folds in these surfaces correspond to singular flux directions.

B. Phonon focusing in piezoelectric crystals

For piezoelectric materials an applied stress produces a strain field *and* an electric field in the crystal. The stress-strain relation is therefore not as simple as before.[14] These effects can be described by the piezoelectric stress equations

$$\sigma_{ij} = C_{ijmn}^E S_{mn} - e_{ijr} E_r , \tag{5a}$$

and

$$D_l = e_{lmn} S_{mn} + \epsilon_{lr}^S E_r , \tag{5b}$$

where e_{ijr} are the piezoelectric stress constants, ϵ_{lr}^S is the dielectric tensor at constant strain, D_l is the electric displacement field, and E_r is the electric field.

We proceed by first assuming no free charge and that at sound velocities magnetic induction can be neglected; that is,

$$\vec{\nabla}\cdot\vec{D} = 0 = \frac{\partial D_l}{\partial x_l} . \tag{6}$$

In the "quasistatic" approximation

$$\vec{E} = -\vec{\nabla}\phi , \tag{7}$$

where ϕ is the electric potential. Now since there is no free charge

$$\frac{\partial D_l}{\partial x_l} = e_{lmn} \frac{\partial S_{mn}}{\partial x_l} + \epsilon_{lr}^S \frac{\partial E_r}{\partial x_l} = 0 ,$$

or

$$e_{lmn} \frac{\partial S_{mn}}{\partial x_l} = \epsilon_{lr}^S \frac{\partial^2 \phi}{\partial x_r \, \partial x_l} . \tag{8}$$

Again, assuming a plane-wave solution

$$\vec{u} = \vec{u}_0 e^{i(\omega t - \vec{k}\cdot\vec{x})} , \tag{9}$$

and

$$\phi = \phi_0 e^{i(\omega t - \vec{k}\cdot\vec{x})} , \tag{10}$$

the right-hand side of Eq. (8) becomes

$$\epsilon_{lr}^S \frac{\partial^2 \phi}{\partial x_r \, \partial x_l} = \epsilon_{lr}^S k_r k_l \phi \equiv \epsilon^{SK} \phi . \tag{11}$$

We now have, using Eq. (8) and the definition of S_{mn} above,

$$E_r = ik_r\phi = ik_r \frac{e_{lmn}}{\epsilon^{SK}} \frac{\partial S_{mn}}{\partial x_l} = -\frac{k_r e_{lmn} k_l}{\epsilon^{SK}} S_{mn} \; . \qquad (12)$$

Using this expression in Eq. (5a), we have

$$\sigma_{ij} = \left[C^{E}_{ijmn} + \frac{k_r e_{ijr} k_l e_{lmn}}{\epsilon^{SK}} \right] S_{mn} \equiv C'_{ijmn} S_{mn} \; , \qquad (13)$$

which defines the stiffened elastic constants, C'_{ijmn}. Table II lists the piezoelectric strain constants and dielectric constants for α-quartz and lithium niobate.

By substituting these wave-vector-dependent elastic constants for C_{ijmn} into the Christoffel equation [Eq. (4)], we can again solve for the constant frequency surfaces and parabolic lines of a given piezoelectric material. Of course, the calculation is much more tedious because it involves computing the first and second derivatives of the $C'_{ijmn} k_m k_n$ with respect to the wave-vector components.[1,16] As in the nonpiezoelectric case, such derivatives are required for determining the group-velocity vector and the Gaussian curvature (i.e., the Jacobian of the $\vec{k}$-to-$\vec{V}$ transformation). We have carried out these calculations for the case of α-quartz[15] and the resulting constant-frequency and wave surfaces are nearly identical to those calculated with unstiffened constants.

For comparison with experimental results, it is useful to make a Monte Carlo simulation of the phonon flux. A large number ($\sim 10^6$) of phonon wave vectors are randomly generated in an isotropic distribution and their corresponding group-velocity vectors are computed and projected onto a viewing surface. Figure 3(a) is such a Monte Carlo image calculated without piezoelectric correction for α-quartz. The viewing surface is normal to the c axis and extends ±56° left to right. To aid in identifying the various structures, Fig. 3(c) is a map of the singular and near-singular structures for the same range of propagation directions. Fast and slow transverse caustics are represented by the thick and thin lines, respectively. The dashed lines are directions of local but nonsingular maxima in flux associated with the slow transverse mode. Local maxima in fast transverse phonon flux can also be found, but they are less pronounced and are not included in the line drawing. Such nonsingular structures have

TABLE II. Room-temperature electroacoustical constants for α-quartz (Ref. 15) and lithium niobate (Ref. 12).

	α-quartz	lithium niobate
Piezoelectric stress constants (C/m^2)	$e_{11}=0.171$	$e_{15}=3.76$
	$e_{14}=-0.0406$	$e_{22}=2.43$ $e_{31}=0.23$ $e_{33}=1.33$
Dielectric permittivity constants (10^{-9} F/m)	$\epsilon^S_{11}=0.0392$	$\epsilon^S_{11}=0.392$
	$\epsilon^S_{33}=0.04103$	$\epsilon^S_{33}=0.247$

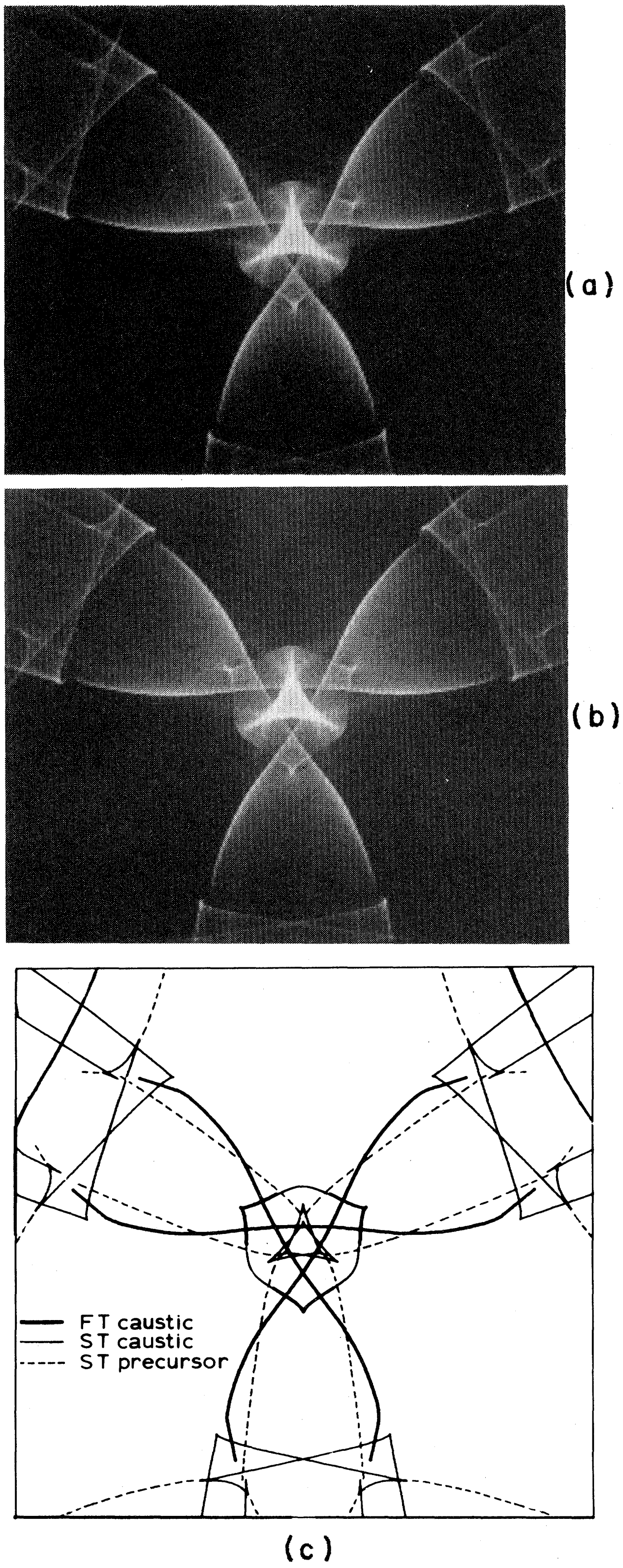

FIG. 3. Monte Carlo image calculation of the phonon-focusing pattern for α-quartz viewed along the c axis. The image extends ±56° horizontally. (a) Piezoelectricity neglected. (b) Piezoelectricity included. (c) A line drawing of the singular and near-singular (precursor) structures of α-quartz viewed along the c axis.

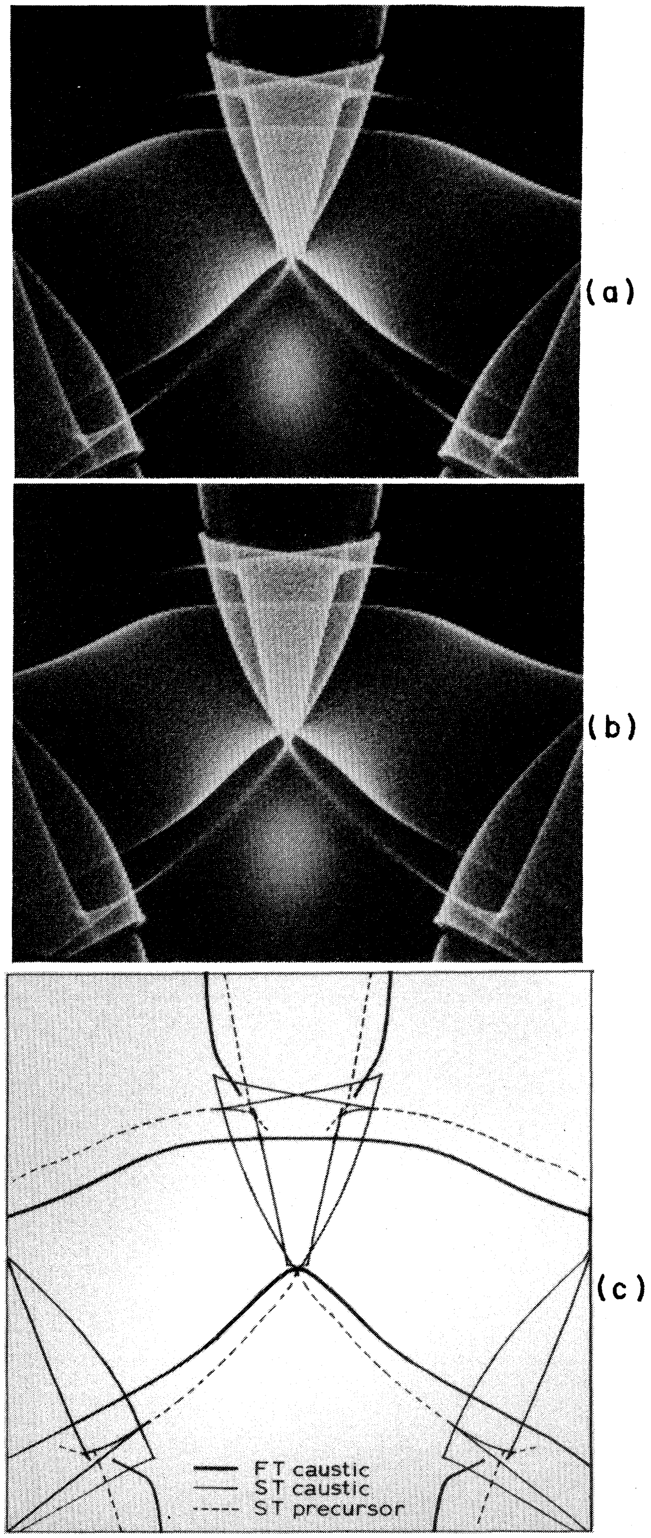

FIG. 4. Monte Carlo image calculation of the phonon-focusing pattern for α-quartz viewed along the $-y$ direction and extending ±56° horizontally. This is equivalent to a viewing surface with normal along the $\phi_v = 30°$ direction in the x-y plane, for comparison with Fig. 2. (a) Piezoelectricity neglected. (b) Piezoelectricity included. (c) A line drawing of the singular and near-singular structures of α-quartz viewed along the $-y$ direction.

previously been called "precursors," because slight changes in elastic constants can change them into singularities.[7]

Figure 3(b) shows the Monte Carlo calculation with piezoelectricity included. It can be seen by comparison with Fig. 3(a) that the changes due to the proper inclusion of piezoelectricity into the calculation are small. Figures 4(a) and (b) show similar Monte Carlo calculations for a different viewing direction, namely along $-y$. This is equivalent to viewing along the $\phi_v = 30°$ direction in the x-y plane, and corresponds approximately to the view of the wave surface shown in Fig. 2. Again it can be seen that the proper inclusion of piezoelectricity to the calculation [Fig. 4(b)] has little effect on the phonon-focusing pattern—for quartz.

III. EXPERIMENTAL RESULTS

The phonon-imaging technique is similar to that used in earlier work.[1,7] A small ($50 \times 50\ \mu m^2$) superconducting Al bolometer, biased to the midpoint of its superconducting transition, provides a sensitive and fast detector of phonon flux capable of 1° angular resolution for our 3-mm-thick samples. The heat source is an argon laser that is focused to a 50-μm spot which is slowly scanned across a copper film evaporated onto the sample. The laser beam is modulated to produce 100—200-ns pulses at a repetition rate of 100 kHz. For a given laser-spot position, the signals are sharp ballistic pulses followed by long tails, which are identified with phonons scattered in the bulk of the crystal (see Fig. 7 and discussion below). For the phonon images a selected time interval is sampled by a boxcar integrator in order to accept fast and/or slow transverse modes over a range of propagation directions. The time-integrated signal, for a given x-y position of the laser spot, is stored in the form of a 256×256 array and displayed on a video monitor for analysis. The resulting images for two α-quartz crystals of different orientation are shown in Figs. 5 and 6.

Figure 5 shows a sequence of time-resolved ballistic phonon images from an α-quartz crystal[17] of dimension $15 \times 15 \times 3\ mm^3$. The laser spot was scanned across one of the larger faces which is oriented perpendicular to the crystallographic c axis. In this case, a 100-ns laser pulse and boxcar gatewidth was used, and several gate delays were chosen to select decreasing phonon velocity. At the earliest time (800 ns), the most intense feature consists of three short spokes radiating from the c axis. This structure is not predicted by the Monte Carlo calculation of Fig. 3, which is based on the constants in Tables I and II. We will discuss the possible origins of this three-spoke feature below. Also, in Figs. 5(a), 5(b), and 5(c) the fast transverse caustic structure predicted in Fig. 3 can be seen. Figures 5(b) and 5(c) show the onset of a triangular feature corresponding to the slow transverse mode. Finally, Fig. 5(d) shows early segments of the slow transverse precursors predicted by the dashed lines in Fig. 3(c). The cusp points at which the precursor lines meet are quite intense, more than predicted by the Monte Carlo calculations. In general, however, the main slow and fast trans-

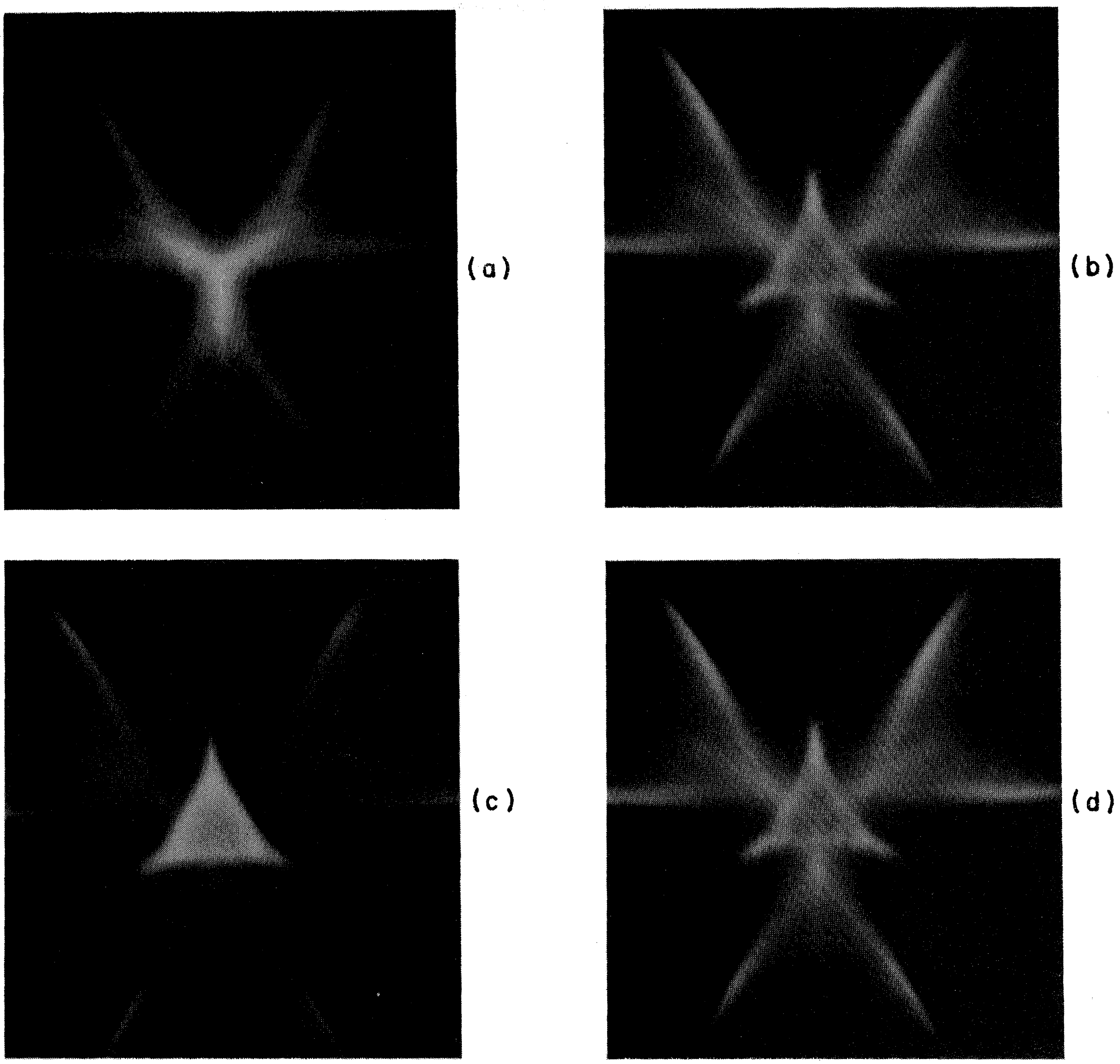

FIG. 5. Experimental ballistic phonon images for a 3-mm-thick crystal of α-quartz with detector and generator surfaces normal to the c-axis. The time gate of the boxcar integrator was 100 ns wide. (a) 800-ns delay after laser pulse, (b) 860-ns delay, (c) 900-ns delay, and (d) 1100-ns delay.

verse structures are well predicted by the above calculation.

Figure 6 shows an experimental phonon image for α-quartz along the negative y axis, or more precisely, the $[0\bar{1}10]$ direction. In this case, a wide (800 ns) boxcar gate was used to collect all of the slow and fast transverse structures. The data is similar to that obtained by Eichele *et al.*[2] using electron beam scanning. Again, the observed phonon-focusing pattern is very close to that predicted by the above theory, as displayed in Fig. 4. There is one additional structure—a small v-shaped feature in the upper-half of the figure—which is not contained in the Monte Carlo calculation. This additional structure, along with the three-spoked feature seen in Fig. 5(a), suggested to us that slight changes in the elastic stiffness constants or piezoelectric constants might be needed to completely describe the phonon-focusing patterns. However, we were not able to produce such features by increasing in turn each of the six elastic constants by as much as 10%. We have also calculated the critical cone channeling directions[7] for our sample orientations, and the resulting patterns do not account for either the early three-spoke feature or the small v-shaped feature. So, presently we have not been able to identify these two observed features.

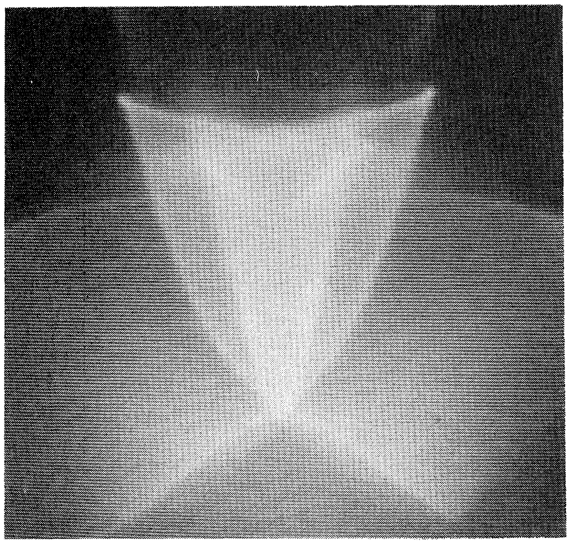

FIG. 6. Experimental ballistic phonon image for 3-mm-thick crystal of α-quartz with detector and generator surfaces normal to the $[1\bar{1}00]$ direction. The time gate was 800 ns wide and delayed 800 ns from the laser pulse.

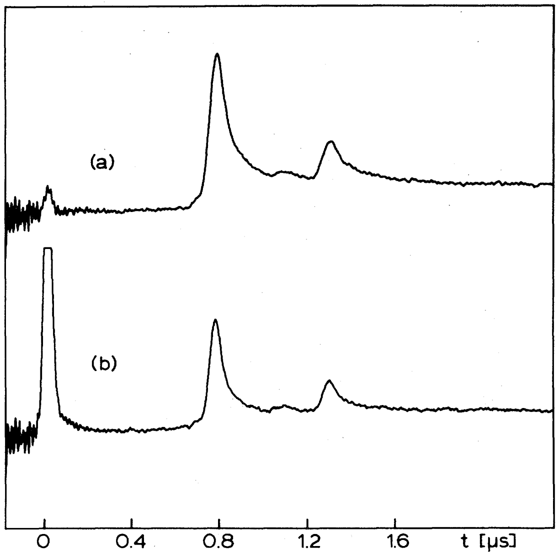

FIG. 7. Time traces of the phonon detector signal showing the transverse phonon peaks. (a) Generator surface covered with a 5000-Å copper film. (b) Generator surface covered with a 500-Å copper film.

Ultimately, we would like to determine experimentally at least a subset of the elastic and piezoelectric constants from the observed focusing pattern, but our analysis technique has not yet evolved to this stage. To reiterate, we have used piezoelectric constants previously determined at room temperature; a reasonable extrapolation to low-temperature values is found to have very little effect on the focusing pattern.

As a technical detail, we show some time traces of heat pulses for an α-quartz sample using a 40-ns laser pulse and a 40-ns boxcar gate. The trace in Fig. 7(a) results from exciting a 5000-Å film of Cu while the trace of Fig. 7(b) is obtained for a 500-Å film of Cu. The laser spot was located at two equivalent directions on the crystal face. The ballistic arrival time is the same but the tail is slightly longer in Fig. 7(a) because the metal film remains hot for a longer period of time. The 15-ns broadening of the phonon pulse implies that the thicker film has an approximately 25-ns response time to the laser pulse. The

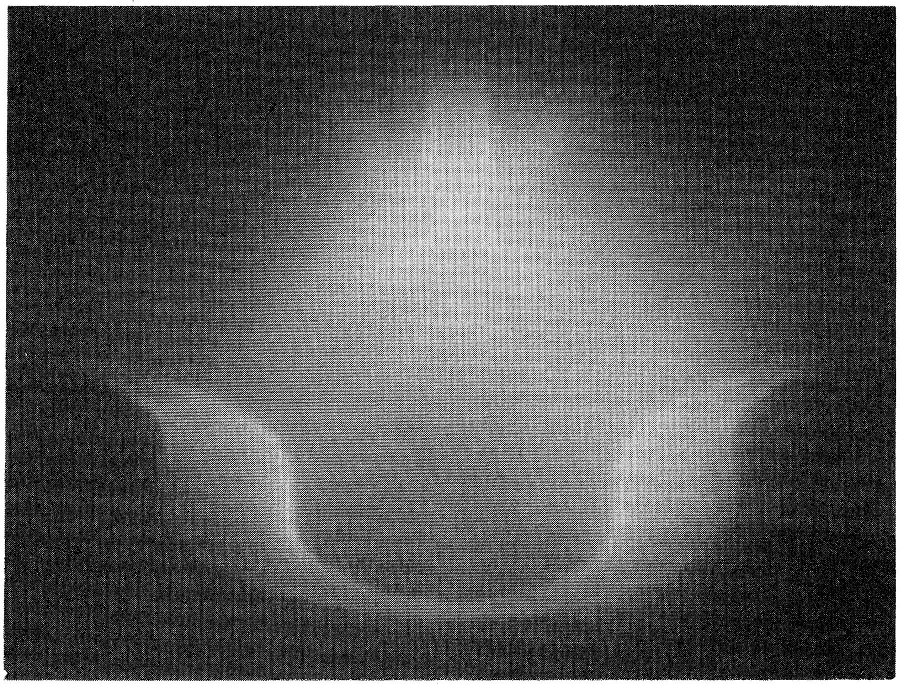

FIG. 8. Experimental ballistic phonon image for lithium niobate, the crystalline orientation is described in the text.

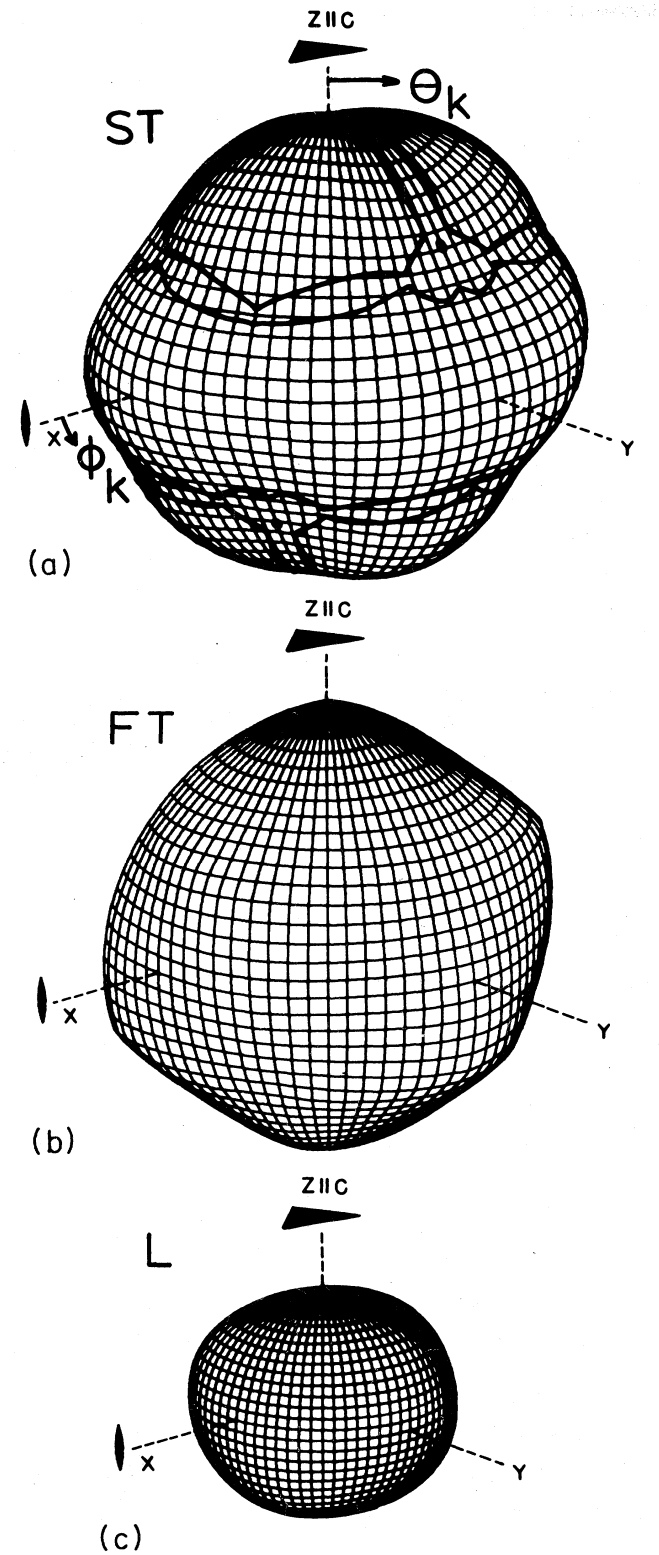

FIG. 9. Constant-frequency surface for lithium niobate, neglecting piezoelectricity. The grid of lines define constant θ_k and ϕ_k at five-degree intervals in the range $-30° \leq \phi_k \leq 150°$ and $0° \leq \theta_k \leq 160°$. The thick lines indicate where the surfaces have zero Gaussian curvature. (a) The ST sheet. (b) The FT sheet. (c) The L sheet.

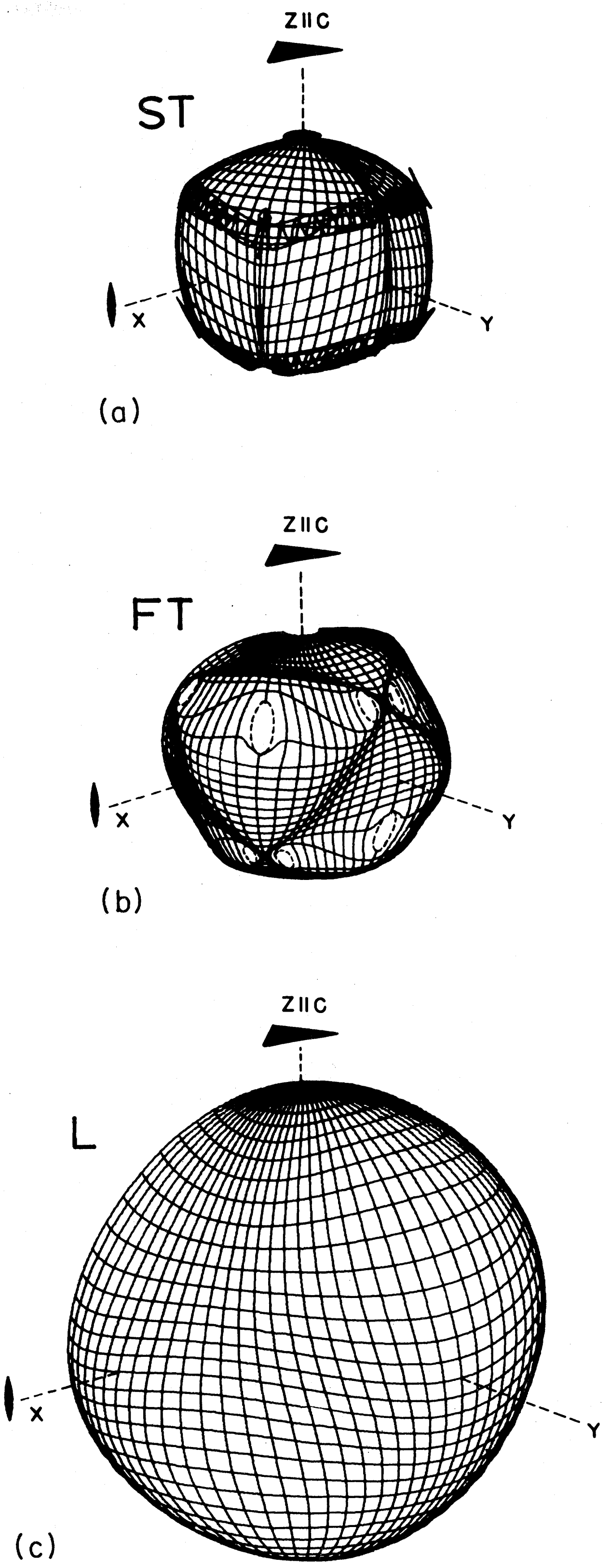

FIG. 10. Wave surface for lithium niobate, neglecting piezoelectricity. The grid of group-velocity vectors define a surface which corresponds to the surface of wave vectors shown in Fig. 9. (a) The ST sheet. (b) The FT sheet. (c) The L sheet.

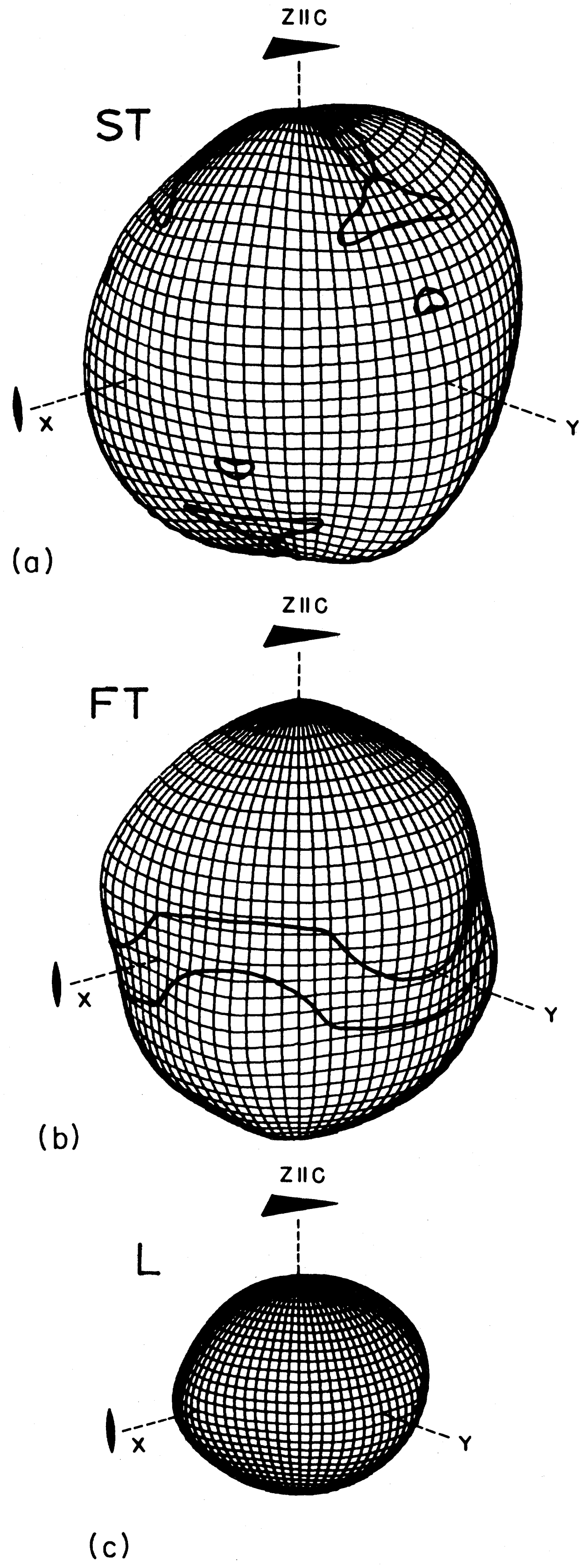

FIG. 11. Constant-frequency surface for lithium niobate including the piezoelectric effect and using the same grid lines as in Fig. 9. (a) The ST sheet. (b) The FT sheet. (c) The L sheet.

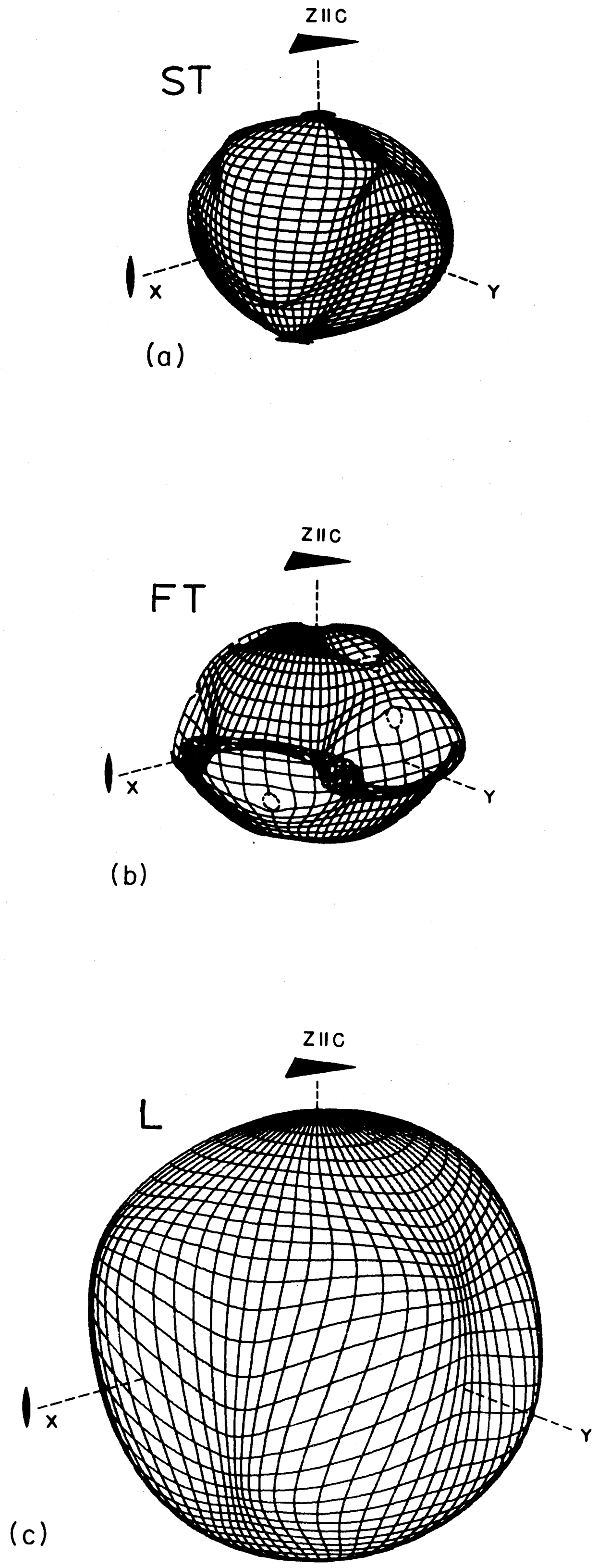

FIG. 12. Wave surface of lithium niobate including piezoelectricity. This is the surface of group-velocity vectors associated with the surface of wave vectors shown in Fig. 11. (a) The ST sheet. (b) The FT sheet. (c) The L sheet.

cooling rate of these metal films is no doubt affected by their contact with superfluid helium as well as with the quartz crystal.

IV. PHONON FOCUSING IN LITHIUM NIOBATE

It has been seen that the effect of piezoelectricity on the ballistic phonon images of α-quartz is almost unnoticeable. We will now investigate the size of this effect in lithium niobate, a piezoelectric material which has found great use as acousto-optical transducers and optical harmonic generators. It has a C_{3v} point symmetry and has considerably larger electroacoustical constants than α-quartz, as listed in Table II.

An experimental phonon image has been obtained for a $LiNbO_3$ crystal of 3 mm thickness with source and detector surfaces normal to $(\theta,\phi)=(37°,90°)$, where, as usual, the angles are defined with respect to the z (threefold) and x (twofold) axes. This is a standard rf transducer crystal[18] which is oriented in this direction for rf coupling purposes: For this cut, rf excitation produces purely longitudinal waves with a large electromechanical coupling factor. Of course, in our heat-pulse experiments all modes are produced at the excitation point. In the phonon image, Fig. 8, a number of sharp structures are observed. This image is a broad scan (about 58° left to right) which includes both slow and fast transverse modes, since a wide (400 ns) boxcar gate was used.

Theoretically, the constant-frequency surface of lithium niobate with piezoelectricity neglected is shown in Fig. 9. To generate this surface, we have used the constant-field elastic constants listed in Table I. The slow transverse sheet in Fig. 9(a) is composed of large totally convex regions bordered by saddle regions and six very small totally concave regions (seen as dots in the figure). Thick lines mark the borders of the regions of different curvature and thus correspond to a total Gaussian curvature of zero. These parabolic lines transform to the fold edges in the wave surface shown in Fig. 10 and indicate directions of mathematically infinite phonon focusing. The constant-frequency FT sheet shows no saddle or concave regions although it has a nearly flat surface near $\theta_k=40°$. This produces a high-intensity precursor of triangular shape about the c axis, as seen in the wave surface, Fig. 10(b). The FT and ST sheets of the constant frequency surface touch each other at several points, called conic points. The symmetry-reduced set of conic points occur at $(\theta_k,\phi_k)=(0,0)$, $(55.9,74.0)$, and at $(64.6,30.0)$. These points produce holes in the FT wave sheet, indicated by dashed lines in Fig. 10(b), and gramophonelike structures in the ST wave sheet. The longitudinal mode displays no singular behavior.

The constant-frequency surface of lithium niobate with piezoelectricity included is shown in Fig. 11, and the corresponding wave surfaces are plotted in Fig. 12. Comparison with Fig. 9 shows that the piezoelectric effect is quite dramatic for this crystal. To see how these topological changes come about, we have made a systematic study of the transverse slowness surface as the piezoelectric constants are gradually introduced. This hypothetical situation was accomplished by simply multiplying all of the piezoelectric constants in Table II by a scale factor f which we varied between zero and one. This corresponds to going continuously from Eq. (1) to Eq. (13). Figure 13 shows a cross section in the y-z plane of the transverse slowness surface for various f. Three major changes can be observed.

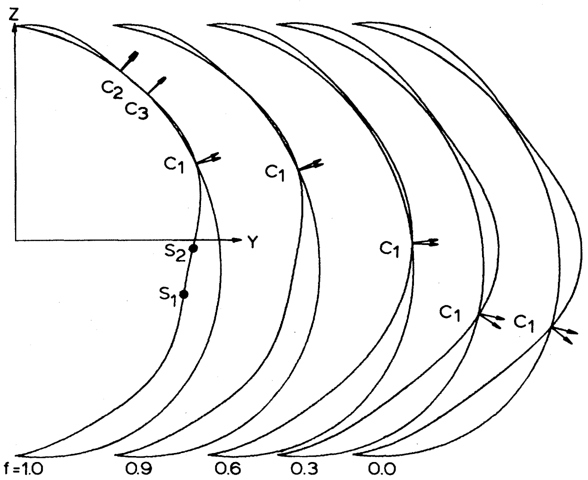

FIG. 13. Cross sections of the $LiNbO_3$ slowness surface through the y-z plane as the piezoelectric stress constants are multiplied by the factor f. The inner and outer sheets are FT and ST modes, respectively. As f is increased, the principal changes are the movement of conic point C_1, the appearance of conic points C_2 and C_3, and the appearance of new singular points S_1 and S_2 on the FT sheet. Singular points on the ST sheet are not shown.

(1) As f is increased, the conic point labeled C_1 begins at $(\theta_k,\phi_k)=(115.4°,90°)$ and moves to $(66°,90°)$ for $f=1$. [Likewise, an equivalent conic point moves from $(64.6°,30°)$ to $(114°,30°)$]. The motions of these conic points coincide with the breakup of the ST saddle region into several sections [Figs. 9(a) and 11(a)].

(2) The ST and FT sheets of this surface touch each other at $\sim(37°,90°)$ when $f=0.95$ and produce two new conic points C_2 and C_3 which move to $(31.1°,90°)$ and $(40.9°,90°)$ for $f=1.0$.

(3) The FT (inner) sheet, which would have no saddle regions for $f=0$, develops a saddle region, bordered by singularities S_1 and S_2, for $f>0.9$.

The remaining conic points outside this symmetry plane also move as f is increased. The conic point at $(55.9°,74.0°)$ annihilates with its mirror twin $(55.9°, -14.0°)$ after they both move to $(\sim 84°,30°)$. We find from this study that the motion of conic points is a useful way to describe the topological changes in an acoustic surface as some control parameter is adjusted. We see that conic points are created or annihilated in pairs.

For $LiNbO_3$ one of the most striking changes introduced with piezoelectric constants is that the fast transverse sheet now has parabolic lines: a large saddle region has developed about the x-y plane and the FT mode now displays singularities in flux!

The substantial distortions in the slowness surface associated with piezoelectricity produce remarkable changes in

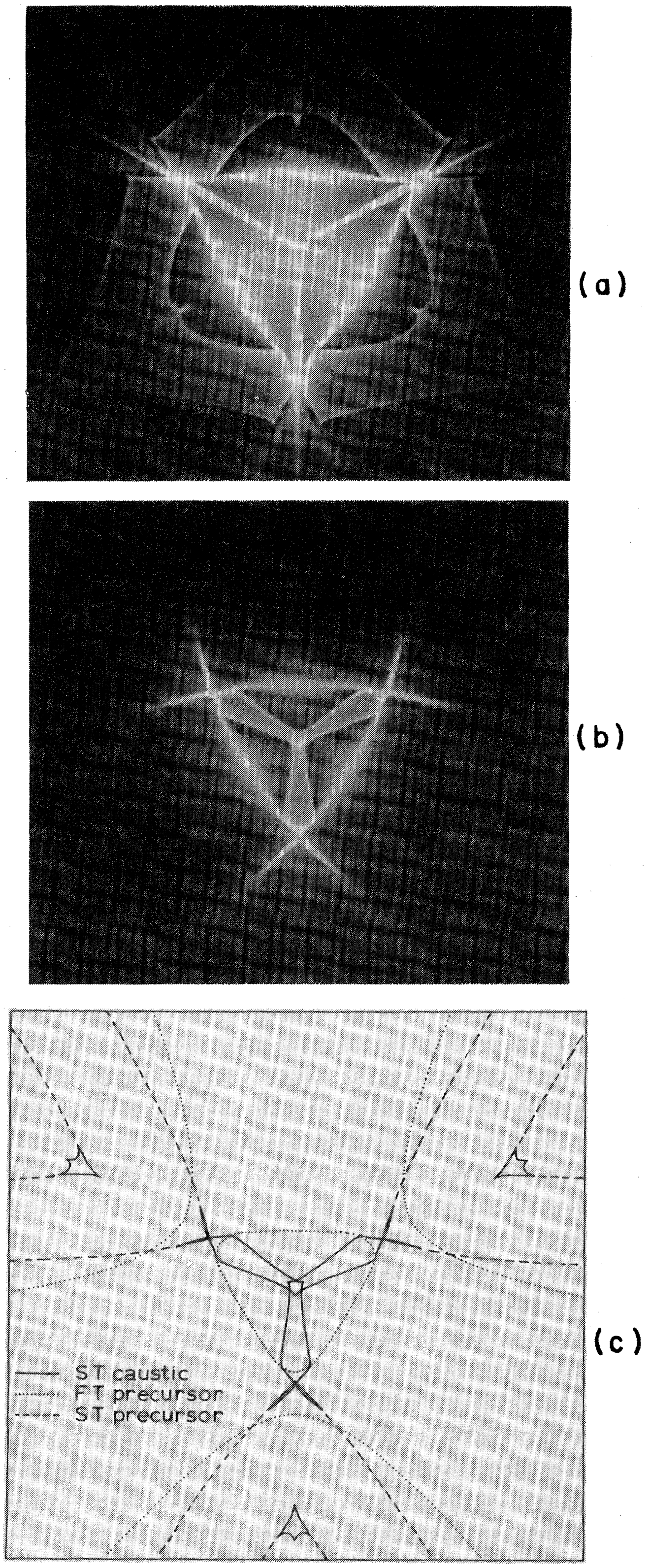

FIG. 14. Monte Carlo calculation of the ballistic phonon-focusing pattern of lithium niobate viewed along the *c* axis and extending ±71° horizontally and vertically. (a) Piezoelectricity neglected. (b) Piezoelectricity included. (c) A line drawing of the singular and near-singular structures of lithium niobate with piezoelectricity included and viewed along the *c* axis.

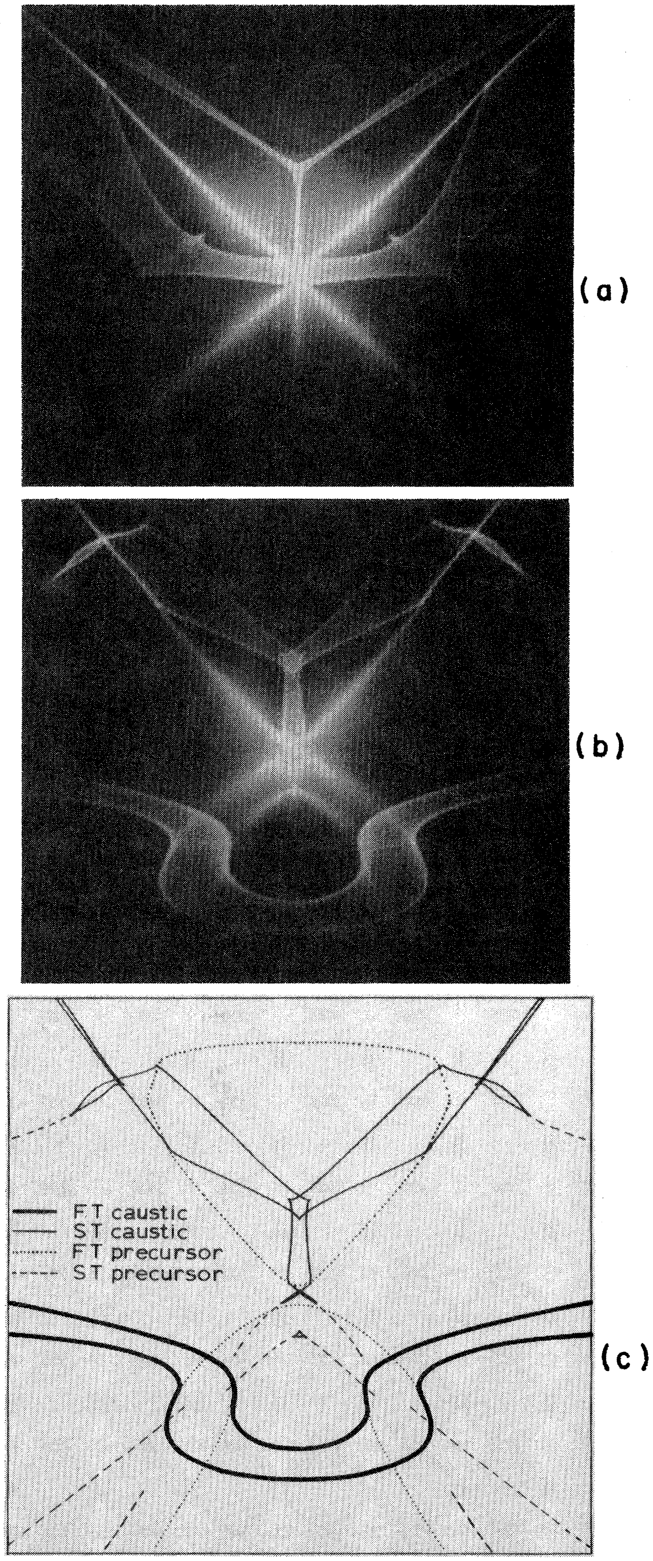

FIG. 15. Monte Caro calculation for the ballistic phonon-focusing pattern of lithium niobate viewed along the direction $\theta_v = 37°$ and $\phi_v = 90°$ extending ±71° horizontally and vertically. (a) Piezoelectricity neglected. (b) Piezoelectricity included. (c) A line drawing of the singular and near-singular structures of lithium niobate with piezoelectricity included and viewed along the same direction.

the predicted phonon-focusing pattern. The wave surface of lithium niobate with piezoelectricity properly included is shown in Fig. 12. Folds are now present in the FT sheet which give rise to singular flux. Monte Carlo calculations for the ballistic heat flux are shown in Figs. 14 and 15, which correspond to two different crystalline orientations. Figure 14 is a view along the crystal c axis at the center, and Fig. 14 corresponds to the experimental crystal orientation in Fig. 8. The intense features occurring in these Monte Carlo calculations can be readily identified with the structures in the wave surfaces of Figs. 10 and 12. Figures 14(a) and 15(a) show the predicted heat flux without taking into account the piezoelectric coupling constants. As expected from the previous considerations of the slowness and wave surfaces, Fig. 15(a) shows very little resemblance to the experimental data of Fig. 8. On the other hand, the calculation of Fig. 15(b), which has piezoelectricity properly included, shows good agreement with the experimental data of Fig. 8. It is clear from this study that piezoelectricity must be properly included in the phonon-focusing calculation in order to understand heat-pulse propagation in this crystal.

V. CONCLUSIONS

In this paper we have extended the calculation of phonon focusing to piezoelectric materials and experimentally examined two such crystals: α-quartz and lithium niobate. Both of these crystals exhibit phonon-focusing patterns with intense singular and nonsingular (precursor) structures.

We have found that while piezoelectricity has only a small effect on the ballistic phonon pattern of α-quartz, it has a very large effect in lithium niobate. In particular, the fast transverse mode in $LiNbO_3$ displays singular structures, which disappear when piezoelectricity is hypothetically removed by reducing the electroacoustical constants to zero. We have examined the topological changes in the slowness surface as these constants are gradually increased and find that the motion of conic points (where FT and ST surfaces touch) provides a means of characterizing the effect of piezoelectricity on wave propagation in crystals.

ACKNOWLEDGMENTS

We thank A. G. Every for suggesting the experiment on lithium niobate[19] and S. E. Hebboul for performing a preliminary phonon-imaging experiment on $LiNbO_3$ which led to the present study. G. A. Northrop provided valuable advice on both experimental and theoretical aspects of this work. This research was supported by the National Science Foundation under the Materials Research Laboratories Program Grant No. DMR-80-20250.

---

[1] G. A. Northrop and J. P. Wolfe, Phys. Rev. Lett. **43**, 1424 (1979); Phys. Rev. B **22**, 6196 (1980).

[2] R. Eichele, R. P. Huebener, H. Seifert, and K. P. Selig, Phys. Lett. **87A**, 469 (1982); R. Eichele, R. P. Huebener, and H. Seifert, Z. Phys. B **48**, 89 (1982).

[3] See reviews by W. Eisenmenger, in *Proceedings of the Third International Conference on Phonon Scattering in Condensed Matter*, edited by H. J. Maris (Plenum, New York, 1980), p. 303; J. P. Wolfe, Phys. Today **33** (12), 44 (1980).

[4] B. Taylor, H. J. Maris, and C. Elbaum, Phys. Rev. Lett. **23**, 415 (1969).

[5] W. Dietsche, G. A. Northrop, and J. P. Wolfe, Phys. Rev. Lett. **47**, 660 (1981); G. A. Northrop, Phys. Rev. B **26**, 903 (1982); S. Tamura, Phys. Rev. B **25**, 1415 (1982); J. P. Wolfe and G. A. Northrop, in *Proceedings of the Fourth International Conference on Phonon Scattering in Condensed Matter*, edited by W. Eisenmenger, K. Lassman, and S. Dottinger (Springer, Berlin, 1984), p. 100.

[6] G. A. Northrop, E. J. Cotts, A. C. Anderson, and J. P. Wolfe, Phys. Rev. B **27**, 6395 (1983); G. A. Northrop, E. J. Cotts, A. C. Anderson, and J. P. Wolfe, Phys. Rev. Lett. **49**, 54 (1982).

[7] A. G. Every, G. L. Koos, and J. P. Wolfe, Phys. Rev. B **29**, 2190 (1984); G. L. Koos, A. G. Every, G. A. Northrop, and J. P. Wolfe, Phys. Rev. Lett. **51**, 276 (1983).

[8] G. A. Northrop and J. P. Wolfe, Phys. Rev. Lett. **52**, 2156 (1984).

[9] A preliminary account of the LiNbo$_3$ results was reported in G. A. Koos and J. P. Wolfe, Phys. Rev. B **29**, 6015 (1984).

[10] E. B. Christoffel, Ann. Mat. Pura Appl. **8**, 193 (1877); see also, A. G. Every, Phys. Rev. Lett. **42**, 1065 (1979).

[11] A. G. Smagin, and B. G. Mil'shtein, Kristallografiya **19**, 832 (1974). [Sov. Phys.—Crystallogr. **19**, 514 (1975)].

[12] R. T. Smith and F. S. Welsh, J. Appl. Phys. **42**, 2219 (1971).

[13] F. Rosch and O. Weis, Z. Phys. B **25**, 101 (1976).

[14] For reviews, see W. G. Cady, *Piezoelectricity* (McGraw-Hall, New York, 1946); B. A. Auld, *Acoustic Fields and Waves in Solids* (Wiley, New York, 1973), Vol. 1, Chap. 8; S. Epstein, Phys. Rev. B **7**, 1636 (1973).

[15] With the use of the piezoelectric stress constants of R. Bechmann, Phys. Rev. **110**, 1060 (1958).

[16] G. A. Northrop, Comput. Phys. Commun. **28**, 103 (1982).

[17] The crystals were cut and polished by Valpey Corp., 1244 Highland St., P. O. Box 145, Holliston, MA 07146.

[18] Crystal grown by Crystal Technology, Palo Alto, CA. We thank W. Baronian of IntraAction Corporation for providing us with this rf-transducer-cut crystal. Our final polishing step was 1-μm diamond polish. The excitation surface was covered with a 2000-Å copper film.

[19] We thank G. Kino for giving us a crystal of $LiNbO_3$ which showed similar phonon images to the reported data.

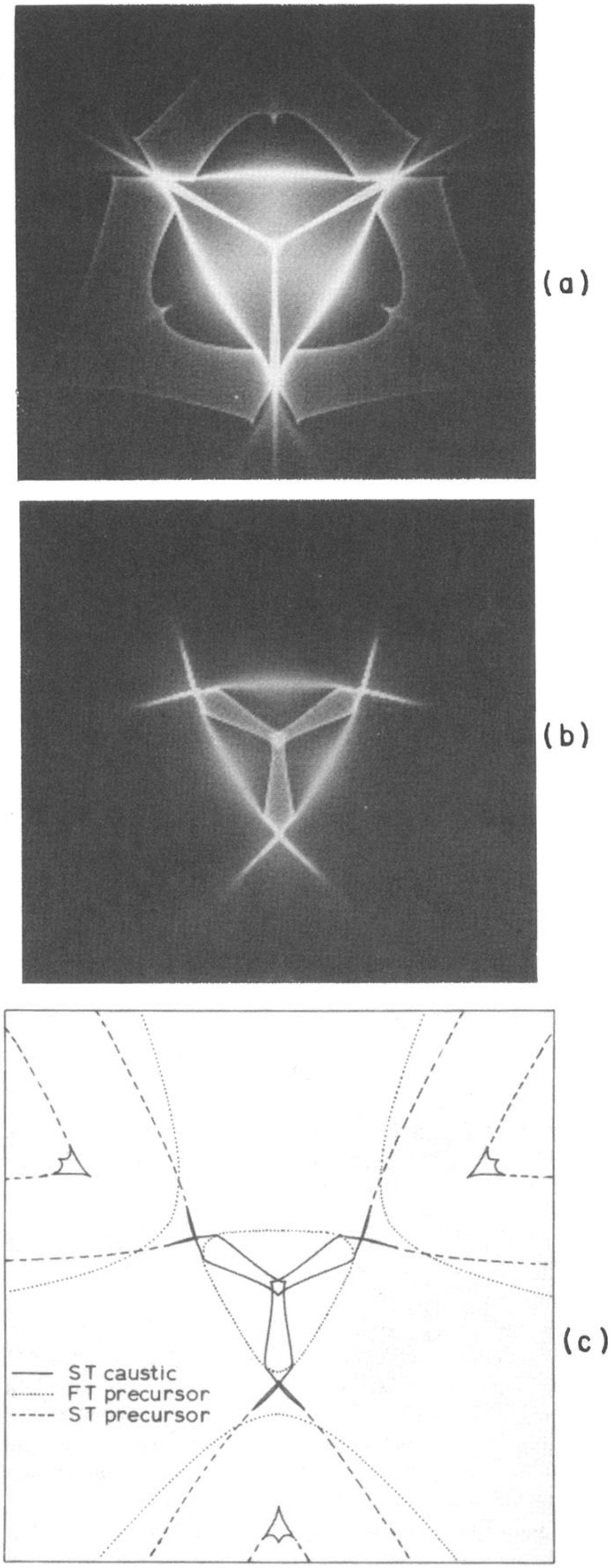

FIG. 14. Monte Carlo calculation of the ballistic phonon-focusing pattern of lithium niobate viewed along the *c* axis and extending ±71° horizontally and vertically. (a) Piezoelectricity neglected. (b) Piezoelectricity included. (c) A line drawing of the singular and near-singular structures of lithium niobate with piezoelectricity included and viewed along the *c* axis.

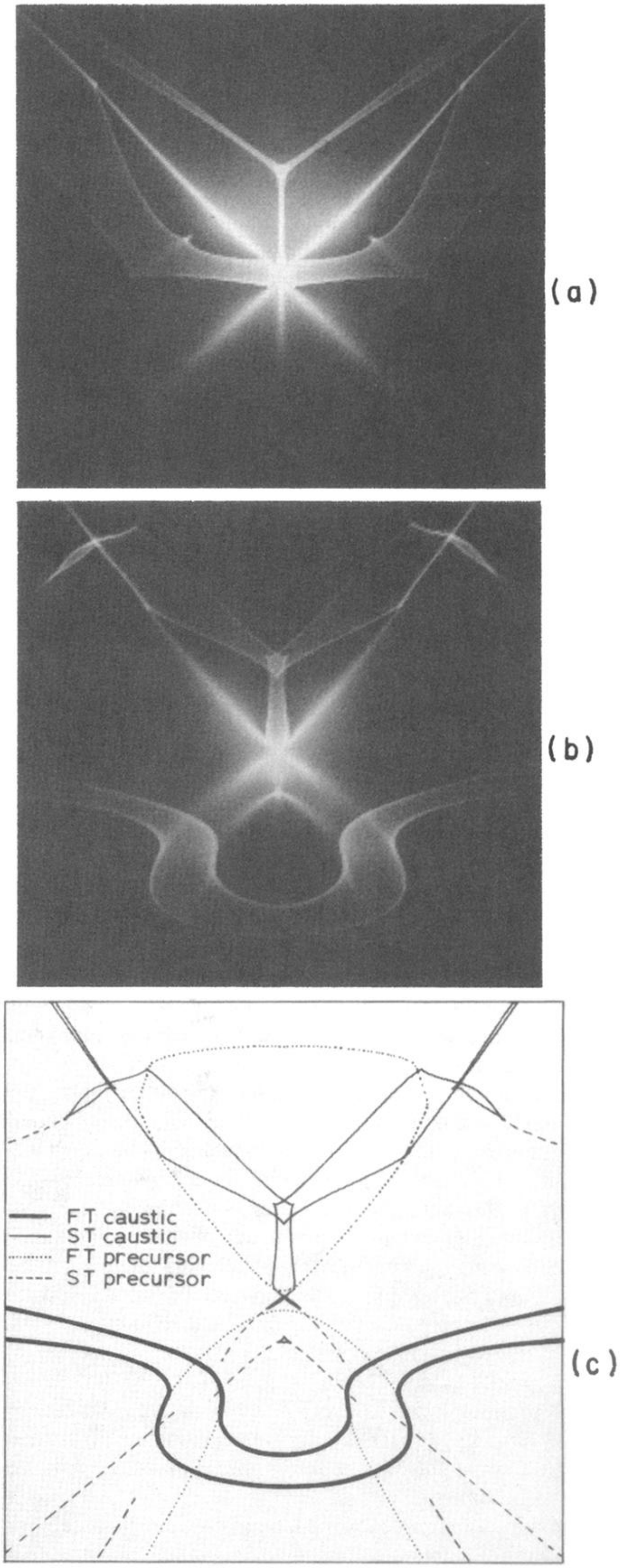

FIG. 15. Monte Caro calculation for the ballistic phonon-focusing pattern of lithium niobate viewed along the direction $\theta_v = 37°$ and $\phi_v = 90°$ extending ±71° horizontally and vertically. (a) Piezoelectricity neglected. (b) Piezoelectricity included. (c) A line drawing of the singular and near-singular structures of lithium niobate with piezoelectricity included and viewed along the same direction.

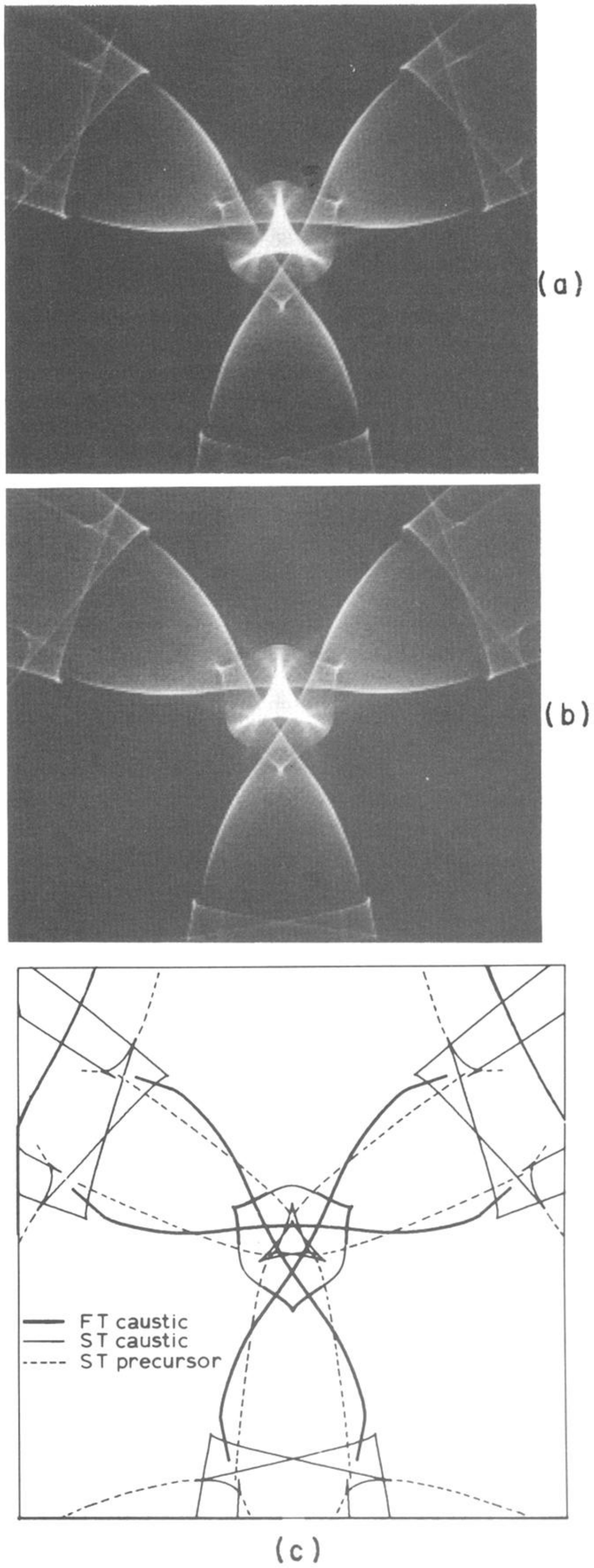

FIG. 3. Monte Carlo image calculation of the phonon-focusing pattern for α-quartz viewed along the *c* axis. The image extends ±56° horizontally. (a) Piezoelectricity neglected. (b) Piezoelectricity included. (c) A line drawing of the singular and near-singular (precursor) structures of α-quartz viewed along the *c* axis.

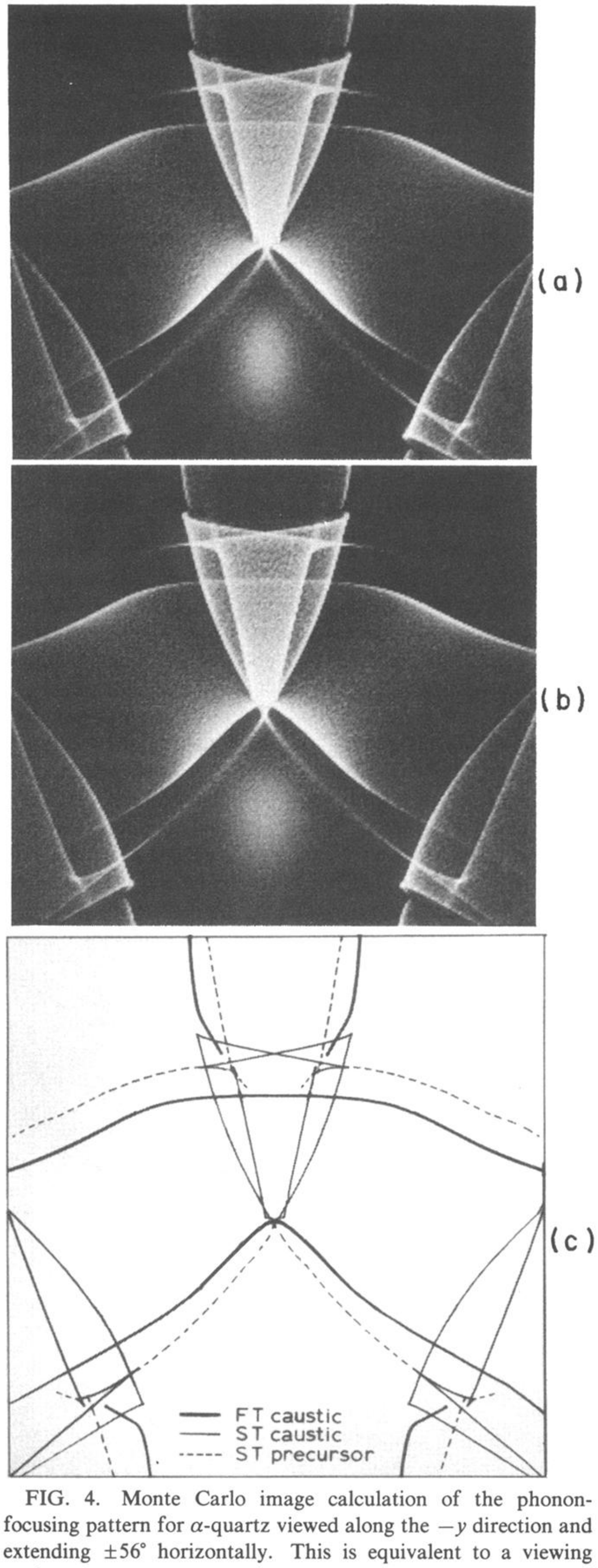

FIG. 4. Monte Carlo image calculation of the phonon-focusing pattern for α-quartz viewed along the $-y$ direction and extending ±56° horizontally. This is equivalent to a viewing surface with normal along the $\phi_v = 30°$ direction in the x-y plane, for comparison with Fig. 2. (a) Piezoelectricity neglected. (b) Piezoelectricity included. (c) A line drawing of the singular and near-singular structures of α-quartz viewed along the $-y$ direction.

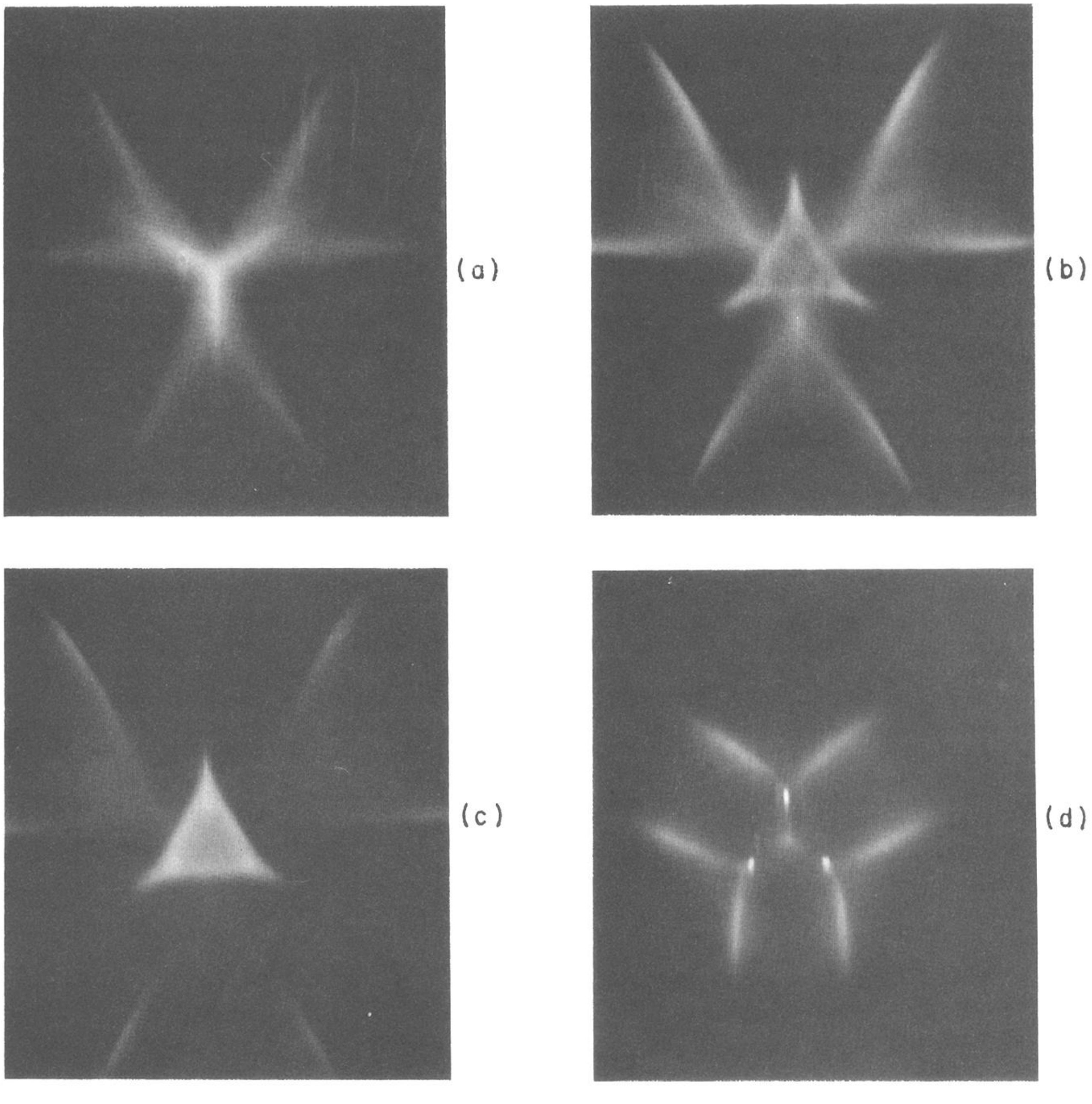

FIG. 5. Experimental ballistic phonon images for a 3-mm-thick crystal of α-quartz with detector and generator surfaces normal to the c-axis. The time gate of the boxcar integrator was 100 ns wide. (a) 800-ns delay after laser pulse, (b) 860-ns delay, (c) 900-ns delay, and (d) 1100-ns delay.

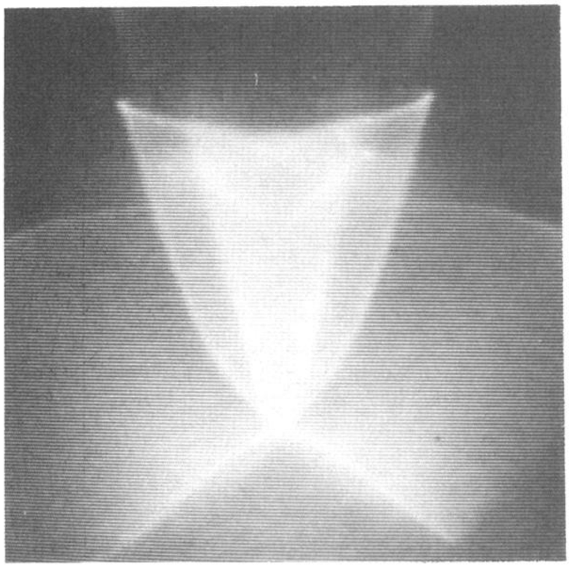

FIG. 6. Experimental ballistic phonon image for 3-mm-thick crystal of α-quartz with detector and generator surfaces normal to the $[1\bar{1}00]$ direction. The time gate was 800 ns wide and delayed 800 ns from the laser pulse.

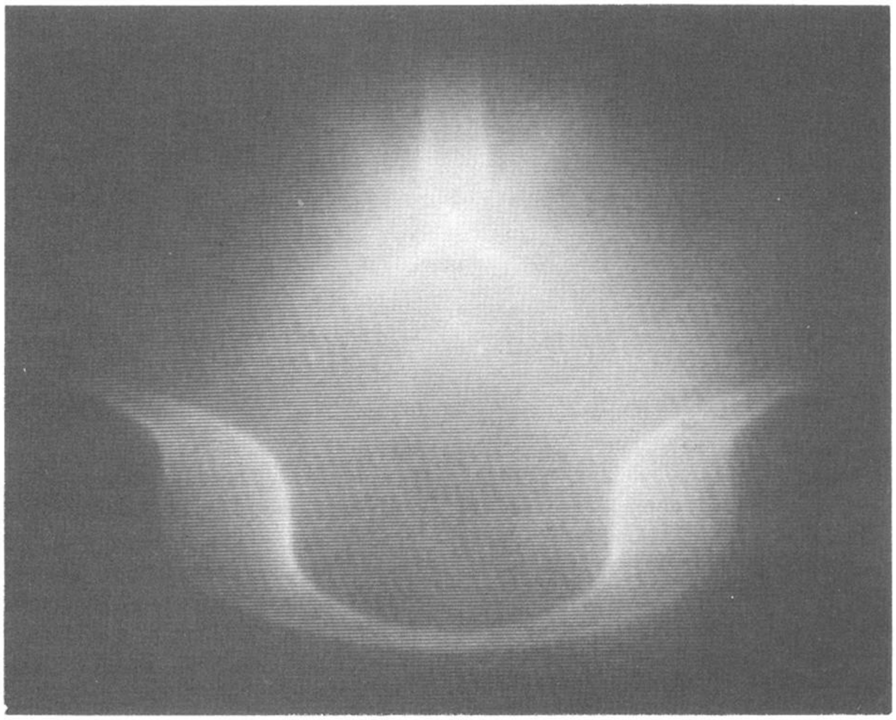

FIG. 8. Experimental ballistic phonon image for lithium niobate, the crystalline orientation is described in the text.